SCIENCE CHINA
Technological Sciences

Special Topic: Erosion and Sedimentation
• Article •

August 2014 Vol.57 No.8: 1500–1511
doi: 10.1007/s11431-014-5606-1

Numerical investigation of particle saltation in the bed-load regime

JI ChunNing[1*], ANTE Munjiza[2], ELDAD Avital[2], XU Dong[1] & JOHN Williams[2]

[1] *State Key Laboratory of Hydraulic Engineering Simulation and Safety, Tianjin University, Tianjin 300072, China;*
[2] *School of Engineering & Materials Science, Queen Mary, University of London, London E1 4NS, UK*

Received December 28, 2013; accepted June 9, 2014

This paper numerically investigates particle saltation in a turbulent channel flow having a rough bed consisting of 2–3 layers of densely packed spheres. In this study, we combined three the state-of-the-art technologies, i.e., the direct numerical simulation of turbulent flow, the combined finite-discrete element modelling of the deformation, movement and collision of the particles, and the immersed boundary method for the fluid-solid interaction. Here we verify our code by comparing the flow and particle statistical features with the published data and then present the hydrodynamic forces acting on a particle together with the particle coordinates and velocities, during a typical saltation. We found strong correlation between the abruptly decreasing particle stream-wise velocity and the increasing vertical velocity at collision, which indicates that the continuous saltation of large grain-size particles is controlled by collision parameters such as particle incident angle, local rough bed packing arrangement, and particle density, etc. This physical process is different from that of particle entrainment in which turbulence coherence structures play an important role. Probability distribution functions of several important saltation parameters and the relationships between them are presented. The results show that the saltating particles hitting the windward side of the bed particles are more likely to bounce off the rough bed than those hitting the leeside. Based on the above findings, saltation mechanisms of large grain-size particles in turbulent channel flow are presented.

particle saltation, bed-load regime, hydrodynamic forces, turbulent channel flow

Citation: Ji C N, Ante M, Eldad A, et al. Numerical investigation of particle saltation in the bed-load regime. Sci China Tech Sci, 2014, 57: 1500–1511, doi: 10.1007/s11431-014-5606-1

1 Introduction

Sediment transport is important for predicting the impact of human intervention on river and coastal systems, which can have large and small scale, and near and far field consequences. In the bed-load layer sediment may be transported via three modes: sliding, rolling and saltation and the last one is considered as the most dominant motion of sediment particles [1,2]. Particle saltation in turbulent channel flow has been experimentally investigated for several decades. Many statistical features, such as saltation length and height, mean particle stream-wise velocity, incidence and take-off angles at collision, and dynamic friction coefficient, etc., have been reported by many researchers [3–12]. However, the hydrodynamic forces acting on the particles and the process of the particles impacting on and rebounding from the rough bed, which plays a fundamental role in particle saltation, have not been studied adequately due to the fact that they are very difficult, if not impossible, to be measured directly.

Besides experimental studies, different theoretical models have also been presented [1,8,9,13]. These models based on Newton's second law and some vital parameters, such as drag and lift coefficients, restitution and friction coefficients, incident and take-off angles, etc., were determined experimentally and reasonable results on the first-order statistics were obtained. However, the fluctuation in particle trajec-

*Corresponding author (email: cnji@tju.edu.cn)

tory caused by the turbulent coherent structures and the diversity of take-off angles owing to the random packing arrangement of particles forming the rough bed were not reproduced in those results. Niño and García [14] stated that neglecting turbulence would lead to the overestimation of the mean values of the saltation length and height. In their numerical study, the turbulent fluid velocity was modeled using a random walk model. Bialik et al. [2] numerically investigated the influence of turbulence structures on the trajectories of saltating particles in an open-channel flow. In their study, the mean flow is 2D and steady. The instantaneous longitudinal fluctuating velocity was generated by using a special procedure based on the assumption that the spectrum of turbulent kinetic energy was known at any distance from the bed. Clearly, these theoretical and numerical studies are quite crude and, basically, the fidelity of the results cannot be guaranteed.

With the development of high performance computer and numerical schemes, sediment transport simulation in which both particles and the turbulent flow field are well-resolved by grids presents an effective way not only to investigate the interaction between particle motions and near-bed turbulence structures, but also to show the dynamic process of particle saltation in detail in which the hydrodynamic forces, collision between particles and pressure distributions on the particle surface are investigated. These results will certainly contribute to the understanding of the underlying physical mechanisms of particle saltation.

Chan-Braun et al. [15] numerically investigated the hydrodynamic forces and torques acting on spherical particles on a rough bed consisting of one layer of spheres in a square arrangement using a combination of the direct numerical simulation (DNS) of the turbulent flow and the immersed boundary method (IBM) for the fluid-solid interactions. Chan-Braun et al. [16] further studied the statistical features of the sediment entrainment in a rough bed channel in which the particles were small and in a suspended load state. However, in their studies, the particles were idealized as rigid spheres and their collisions and resulting contact forces were calculated using an artificial repulsion potential. It is common knowledge that the collision process, although short in time, is very complicated and crucial to the particle saltation. Thus, the over-simplified models such as that used in Chan-Braun et al. [16] may lead to unexpected results. To avoid this problem, we applied the combined finite-discrete element method (FDEM) for the particle dynamics, in which the deformability of the particles was taken into account by solving the kinematic relations and the constitutive equations, while particle collisions were modelled using the penalty function method.

This study is aimed at determining the statistical features of particle saltation in turbulent channel flow and the underlying physical mechanisms. It differs from the experimental studies of refs. [4,6,7] in that a complete dynamical process of the continuous particle saltation in a surrounding turbulent flow is presented for the first time. The closely correlated decreasing stream-wise velocity and increasing vertical velocity of a saltating particle at collision, together with the time histories of the hydrodynamic forces, show clear evidence that large particles obtain vertical momentum mainly from their stream-wise momentum. The probability distribution functions (PDF) of several important particle saltation parameters (such as the incident, rebound and collision angles, the incident, rebound and saltation velocities, etc.) and the relationships between them, which were not sufficiently investigated in the experimental studies, are also presented. It should be noted that the turbulent flow and the interactions between flow and particle are numerically simulated on the well-resolved grids which is totally different from previous theoretical models [1,8,9,13] in which the turbulence was modelled and the fluid-solid interaction neglected. Compared with the numerical simulation of Chan-Braun et al. [15,16], the use of FDEM guarantees the fidelity of the simulation of complex interactions among the saltating particles and the rough bed.

2 Methodology

The whole problem can be divided into three sub-problems, i.e. the simulation of turbulent channel flow, the simulation of particle movement, deformation and collision, and the simulation of the interaction between turbulent flow and particle motion. Accordingly, the methodology applied in this study is a combination of three state-of-the-art numerical technologies, i.e. DNS of the turbulent flow, the FDEM for the particle dynamics, and the IBM for the fluid-solid interactions.

The code used to simulate the turbulent flow is an in-house computational fluid dynamics (CFD) C code called CgLes [17]. It is a 3D DNS/LES (large eddy simulation) code with second order accuracy in both time and space. This code was applied to simulate turbulent flow over a rough bed in our previous work [18,19] and has a proven high fidelity and parallelizing efficiency.

The immersed boundary method, first introduced by Peskin [20] in the simulation of blood flow around the flexible leaflet of human heart, was incorporated into CgLes to model the interaction between the flow and moving particles. In the IBM framework, the flow governing equations are discretized on a fixed Cartesian grid which generally does not conform to the geometry of moving solids. As a result, the boundary conditions on the fluid–solid interface which manifest the interaction between fluid and solid cannot be imposed straightforwardly. Instead, the solid surface is represented by a set of immersed boundary points (IBPs) on which an extra singular body force is imposed. This force is then added into the momentum equation of fluid motion to take such fluid-solid interaction into account using interpolation/distribution functions.

The conservative forms of the second-order Adams-Bashforth temporal-discretized governing equations of incompressible fluid flow using the IBM are

$$\boldsymbol{u}^{n+1} = \boldsymbol{u}^n + \delta t\left(\frac{3}{2}\boldsymbol{h}^n - \frac{1}{2}\boldsymbol{h}^{n-1} - \frac{3}{2}\nabla p^n + \frac{1}{2}\nabla p^{n-1}\right) + \boldsymbol{f}^{n+\frac{1}{2}}\delta t \tag{1}$$

and

$$\nabla\cdot\boldsymbol{u}^{n+1} = 0, \tag{2}$$

where, $\boldsymbol{u}$ is the fluid velocity, p is the pressure and $\boldsymbol{h} = \nabla\cdot(-\boldsymbol{uu} + \nu(\nabla\boldsymbol{u} + \nabla\boldsymbol{u}^t))$ are the convective and diffusive terms. The extra body force $\boldsymbol{f}$ on the Cartesian grids is defined as

$$\boldsymbol{f}^{n+\frac{1}{2}} = \frac{1}{\delta t}D\left(\boldsymbol{V}^{n+1} - I\left(\boldsymbol{u}^n + \delta t\left(\frac{3}{2}\boldsymbol{h}^n - \frac{1}{2}\boldsymbol{h}^{n-1} - \frac{3}{2}\nabla p^n + \frac{1}{2}\nabla p^{n-1}\right)\right)\right), \tag{3}$$

where I and D represent the interpolation and distribution functions, respectively, $\boldsymbol{V}$ is the velocity of the IBPs which is determined by the motion of the solids.

The main advantage of the IBM is associated with its inherent simplicity in treating flows which have solids with moving boundaries due to the fact that the IBPs are not connected with the Cartesian background grid. To improve the accuracy of the IBM, an iterative direct-forcing IBM which was introduced in our previous work [21] is applied in this study.

To simulate the movement and collision of particles, the FDEM developed by Munjiza et al. [22] was applied. In the context of the FDEM, each particle of general shape is represented as a single discrete element which is then discretized into finite elements for deformability, fracture and fragmentation. The movement of particles is simply governed by the Newton's second law. The penalty function method is employed to calculate the normal contact force $\boldsymbol{F}_n$ when two particles are in contact and assumes that the two particles penetrate each other. Because the discrete elements are discretized into finite elements, each contacting pair of discrete elements is in fact represented by a set of contacting finite elements. The elemental contact force is then directly related to the overlapping area of the finite elements in contact. In this study, a distributed contact force algorithm introduced by Munjiza and Andrews [23] - which is relatively easy to implement and preserves energy balance - is applied to generate a realistic distribution of contact forces over finite contact areas. The calculated elemental contact force is then distributed around the nodes surrounding the contact in order to preserve the system from artificial stress concentration.

As suggested by Munjiza and Andrews [23], the normal contact force is given by

$$\boldsymbol{F}_n = \sum_{i=1}^{n}\sum_{j=1}^{m}\int_{\Gamma_{\beta_{ci}\cap\beta_{tj}}} \boldsymbol{n}_{\Gamma_{\beta_{ci}\cap\beta_{tj}}}(\varphi_{ci} - \varphi_{tj})d\Gamma, \tag{4}$$

where, β_{ci} and β_{tj} are the i th and j th finite elements of the contactor and target discrete elements respectively, while n and m are the total number of finite elements into which the contactor and target discrete elements are discretized. $\boldsymbol{n}_{\Gamma_{\beta_{ci}\cap\beta_{tj}}}$ is the outward unit normal to the boundary Γ of the overlapping volume $\beta_{ci}\cap\beta_{tj}$. φ_c and φ_t are potential functions for the contactor and target discrete elements respectively.

In this study, the simplest finite element in 3D - a linear four-node tetrahedron-has been adopted. The potential function at an arbitrary point P inside a tetrahedral finite element is given by

$$\varphi(P) = 4k_p\min\{V_1/V, V_2/V, V_3/V, V_4/V\}, \tag{5}$$

where k_p is the penalty parameter, V the volume of the tetrahedral finite element and V_i $(i = 1,2,3,4)$ are the volumes of the corresponding sub-tetrahedrons at the point P. The potential φ equals 1 at the tetrahedron center and 0 at and beyond the tetrahedron surfaces.

Xiang et al. [24] further developed the FDEM by taking into account the sliding friction force by implementing the well-known Coulomb-type friction described as follows:

$$\boldsymbol{F}_t = -k_t\boldsymbol{D}_t - \eta_d\boldsymbol{V}_t, \tag{6}$$

in which $\boldsymbol{F}_t$ is the tangential elastic contact force, k_t the tangential spring stiffness constant, η_d the viscous damping coefficient and $\boldsymbol{D}_t$ and $\boldsymbol{V}_t$ are the tangential relative displacement and velocity between particles respectively. If $\boldsymbol{F}_t$ is bigger than the friction force obeying the Coulomb-type friction law, i.e., $|\boldsymbol{F}_t| > \mu|\boldsymbol{F}_n|$, the particles slide over one another and the tangential force is then calculated using the total normal elastic contact force $\boldsymbol{F}_n$:

$$\boldsymbol{F}_t = -\mu|\boldsymbol{F}_n|(\boldsymbol{V}_t/|\boldsymbol{V}_t|), \tag{7}$$

where μ is the coefficient of sliding friction.

The FDEM code therefore includes algorithmic procedures for deformability of individual discrete elements, fracture and fragmentation algorithms (switched off for this study), contact detection between moving solids, frictional-sliding interaction between solids and a whole set of application specific algorithms.

3 Validation of flow and saltation statistics

In this study, we considered sediment transport in a fully

developed turbulent open channel flow having a rough bed consisting of 2–3 layers of densely packed spheres, as shown in Figure 1. The total number of spheres is 6355 and the rough bed is water-worked which means the most exposed spheres are removed. This sphere arrangement [25] was provided by researchers in TU Delft. No-slip boundary conditions have been used on both the bed and sphere surfaces and the top boundary is set as a free-slip hard lid. Periodicity is imposed in the stream-wise and span-wise directions. Table 1 summarizes the simulation parameters.

The computations were run on the UK's national supercomputing facility: HECToR. This simulation was carried out on 150 processors (AMD Opteron 2.3 GHz) for a wall-clock time of 2 months, which is about 200K CPU hours.

In order to keep the computational requirements to a minimum, we first carried out a LES at one half of the DNS grid resolution with fixed spheres. The LES was run for around 30T (where $T = d / u_\tau$ is the large-eddy turnover time) to obtain a fully developed turbulence flow. This fully developed turbulent flow field was then interpolated onto the DNS grid to yield the initial conditions for the DNS. Time integration was performed on the DNS grid for 20T to make the effect of the initial conditions vanish and for the velocity field to reach a fully developed state. The mean

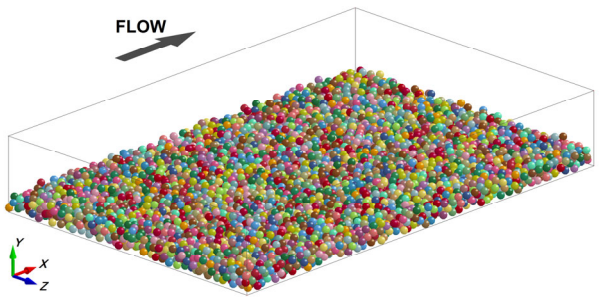

Figure 1 Channel geometry.

Table 1 Parameters of the bed-load transport simulation

Item	Value
Computational box size	$6d \times d \times 4d$
Reynolds number	$Re^+ = u_\tau d / \nu = 1000$
DNS grid	$960 \times 160 \times 640$
Grid resolution	$\Delta x^+ = \Delta y^+ = \Delta z^+ = 6.25$
Kolmogorov length scale	$\eta^+ \approx 3.3$
Height of roughness elements	$k = 0.3d$
Density ratio	$s_s = \rho_s / \rho_f = 2.65$
Particle diameter	$D = 0.1d$
Particle Reynolds number	$Re_D^+ = u_\tau D / \nu = 100$
Shields function	$\Theta = \tau_w / (gD(\rho_s - \rho_f)) = 0.065$

Note: d is the channel depth, u_τ is the flow friction velocity, ν is the kinematic viscosity of fluid, ρ_s and ρ_f are the density of solid and fluid, respectively, τ_w is the non-dimensional bed shear stress on the effective bed location, g is the gravitational acceleration.

velocity profiles and turbulent quantities were then calculated over a further 10T. Once the turbulence was statistically stable, time was reset to zero and the spheres were then set free. The spheres' motions together with the surrounding flow field were recorded for 12T. Various saltation statistics began to be calculated at t = 6T after which the movements of the spheres were considered to be statistically stable.

To facilitate the discussion below, the following terminology is adopted: Single-phase flow indicates the turbulent channel flow over a fixed rough bed and the two-phase flow denotes the turbulent channel flow with sediment transport.

3.1 Turbulent flow statistics

To verify our results, we compared the temporal and plane averaged statistics obtained from the DNS with the experimental data of Defina [26], Grass et al. [27], Grass [28], Nezu [29] and the numerical results of Singh et al. [18].

An approach of fitting mean velocity curve to the logarithmic law-of-the-wall was applied to determine the effective bed location y_b and the equivalent bed roughness height k_s by solving a two-parameter nonlinear curve-fitting problem using the least squares and Newton-Raphson techniques. This procedure yields y_b = 0.84k, k_s = 0.807k and a roughness Reynolds number of $k_s^+ = 242$ indicating a completely rough flow regime. This set of values is in a good agreement with the experimental data (y_b = 0.783k and k_s = 0.88k with $k_s^+ = 79.2$) of Defina [26] and the numerical results (y_b = 0.81k and k_s = 0.768k with $k_s^+ = 102$) of Singh et al. [18]. The distance between the effective bed location and the highest crest of the roughness elements in this simulation is $\delta/k = 0.16$ which is close to the lower bound of the suggested range $\delta/k = 0.15 - 0.3$ of Nezu and Nakagawa [30]. Table 2 lists the mean flow features computed based on the DNS data.

In order to compare the DNS results with those from the literature, a vertical coordinate $Y = y - y_b$ is defined. Figure 2 shows the mean stream-wise velocity profile over the rough bed. Good agreement with the measured data of Defina [26] ($k_s^+ = 288$) has been achieved. The deviations from the experimental data of Grass et al. [27] and the DNS results of Singh et al. [18] are obviously due to the different

Table 2 Mean flow features obtained from the DNS data for the single-phase flow

Flow variables	Reynolds number
Equivalent roughness, $k_s = 0.807k$	$k_s^+ = k_s u_\tau / \nu = 242$
Effective channel depth, $h = d - y_b = 2.493k$	$Re_h^+ = u_\tau h / \nu = 748$
Bulk mean velocity, $U_b = 8.578u_\tau$	$Re_b^+ = U_b h / \nu = 6417$
Mean velocity of the top surface, $U_c = 10.80u_\tau$	$Re_c^+ = U_c h / \nu = 8078$

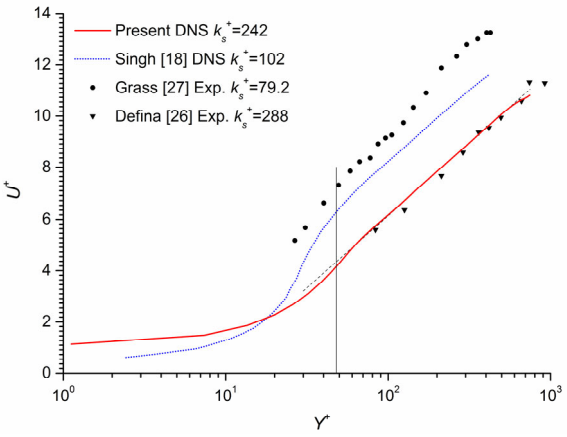

Figure 2 (Color online) Mean velocity profiles. The dashed line indicates the logarithmic law-of-the-wall with $k_s^+ = 242$ and the vertical solid line represents the highest crest of the roughness elements.

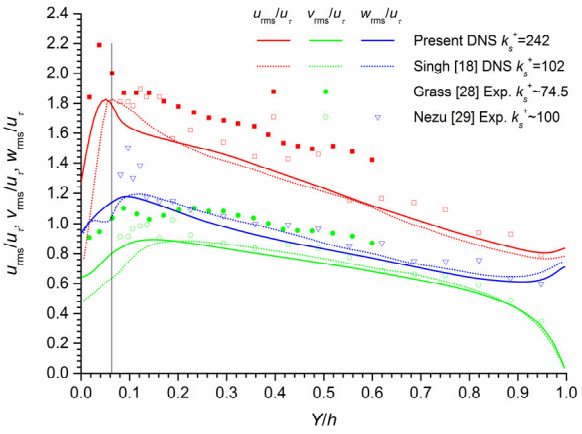

Figure 4 (Color online) Turbulence intensities. The vertical solid line represents the highest crest of the roughness elements.

roughness adopted. However, these profiles collapse when they are plotted against Y/k_s (Figure 3) to eliminate the roughness effects on the velocity profile.

Figure 4 shows the turbulence intensities together with the experimental values from Grass [28] and Nezu [29] and the DNS results of Singh et al. [18] with roughness Reynolds numbers of 74.5, 100 and 102, respectively. It can be seen that the present values are lower than the experimental data of Grass [28] and Nezu [29], but show fairly good agreement with the DNS results of Singh et al. [18] everywhere except near the rough bed. The peak value of 1.84 of the stream-wise velocity fluctuation $u_{\rm rms}/u_\tau$ compares well with 1.83 obtained by Singh et al. [18] but both are lower than the published experimental results, e.g., $u_{\rm rms}/u_\tau$= 2.2 in Grass [28], and is due to the different definitions of u_τ used. In the experimental work of Grass [28], u_τ is defined as the friction velocity on the effective bed location of a rough bed. However, in the DNS study of Singh et al. [18], u_τ is calculated as $\sqrt{\tau_b / \rho_f}$, where τ_b is the shear stress estimated using a linear extrapolation of the total shear stress profile to the smooth channel bed. In this study, the definition of Singh et al. [18] is used for the convenience of comparison. However, if Grass's definition is used the peak values of $u_{\rm rms}/u_\tau$ become 2.05 and 2.13 respectively for Singh et al. [18] and the present simulation thus giving much closer agreement. Correspondingly, the corrected grid resolution of the present study becomes 5.4 wall units in all the three directions. It should also be mentioned that these peak values are significantly lower than the values of around 2.8 for turbulent flow over smooth wall. As stated in ref. [31], large roughness elements destroy the near-wall cycles of coherent flow and thus result in a reduced near-wall peak. Moreover, the random arrangement of spheres used in this study further contributes to a lower peak value due to the irregular rough-bed surface having a similar effect to large roughness elements in destroying near-wall coherent structures.

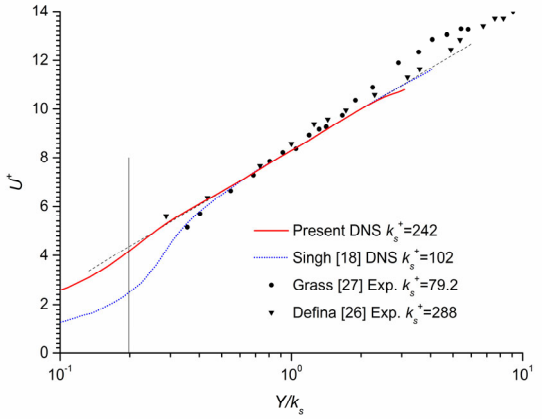

Figure 3 (Color online) Mean velocity profiles plotted against Y/k_s. The dashed line indicates the logarithmic law-of-the-wall with $k_s^+ = 242$ and the vertical solid line represents the highest crest of the roughness elements.

3.2 Particle saltation statistics

We first calculated the turbulence statistics of the two-phase flow. y_b and k_s were determined using the same method described above. However, k is uncertain in the two-phase case due to the changing value of the highest crests of the spheres. We tried different values of k from zero to 0.5d and found $k = 0.35d$ could generate the best curve-fitting results, i.e., $y_b = 0.754k$ and $k_s = 0.834k$. The roughness Reynolds number for the two-phase case is $k_s^+ = 292$. The distance between the effective bed location and the height of the roughness elements is $\delta/k = 0.246$. Table 3 lists these values together with other mean properties computed based on the DNS data. For the details of the velocity profiles and turbulent intensities of the two-phase flow refer to our previous study [32].

We then further verified the statistical features of particle saltation. Table 4 shows the comparison between experimental data and our numerical results. The mean non-dimensional particle saltation length λ_s/D and its standard

Table 3 Mean flow features obtained from the DNS data for the single-phase flow

Flow variables	Reynolds number
Equivalent roughness, $k_s = 0.834k$	$k_s^+ = k_s u_\tau / \nu = 292$
Effective channel depth, $h = d - y_b = 2.103k$	$Re_h^+ = u_\tau h / \nu = 736$
Bulk mean velocity, $U_b = 8.259u_\tau$	$Re_b^+ = U_b h / \nu = 6079$
Mean velocity of the top surface, $U_c = 10.43u_\tau$	$Re_c^+ = U_c h / \nu = 7676$

deviation of our results show good agreement with the experimental data of Niño and García [6] (referred to as N&G hereafter) and Abbott and Francis [4] (referred to as A&F hereafter) with the transport stages $\tau_w/\tau_{wc} = \Theta/\Theta_c$ of all the three cases slightly above 1.0, where τ_{wc} and Θ_c are the critical bed shear stress and Sheilds number for sediment motion, respectively. It should be noted that the grain size of the three cases differs significantly (natural sand particles with D = 0.53 mm and $Re_D^+ = 10.6$ in N&G, ellipsoidal pea-gravel with a nominal diameter D = 8.28 mm and $Re_D^+ = 523$ in A&F and spheres with $Re_D^+ = 100$ in our case), which means the non-dimensional saltation length λ_s/D is insensitive to the particle size. A similar conclusion can be deduced for the non-dimensional particle saltation height h_s/D although our numerical results are a little lower than those of the experimental data. The non-dimensional stream-wise velocity of particle saltation u_s/u_τ shows a clear dependency on grain size. For large particle sizes, our numerical results agree well with the data of the gravel transport experiments with D = 3.3 mm and $Re_D^+ = 150$ of Luque and van Beek [33] and the calculated value using the regression equation recommended. However, the stream-wise velocity increases with decreasing grain size, e.g., $u_s = 4.26$ for the case with D = 0.9 mm and $Re_D^+ = 19.9$ of Luque and van Beek [33] and $u_s = 5.95$ for the case with D = 0.53 mm and $Re_D^+ = 10.6$ of N&G. This could be attributed to the fact that large size particles need more momentum to reach a high stream-wise velocity. The rebound (take-off) angle θ_r and incident angle θ_i of the particle saltation trajectory of the present results are much higher than those of N&G. This is a result of the smaller grain size applied in their test. In fact, in the gravel saltation experiments of Niño et al. [7], the take-off and incident angles are 39.0° and 25.1° (obtained by extrapolating the regression linear line to $\tau_w/\tau_{wc} = 1.0$ using Figure 15 of N&G), respectively, which are quite close to our numerical values. The mean dynamic friction coefficient $\mu_d = (1+R)\tau_w \Delta u_s u_s/\lambda_s$ of our numerical results is 0.158 which agrees well with 0.159 of N&G, where $R = s_s - 1$ is the submerged particle specific density and Δu_s is the non-dimensional stream-wise particle velocity change at collision. Other validations on the sediment concentration profile, particle volumetric flux density and sediment transport rate can be found in our previous study [32]. On the whole, the statistics obtained from the DNS data shows excellent agreement with the experimental values and gives strong evidence of the high accuracy and fidelity of our numerical results.

4 Dynamic process, statistical features and mechanisms of particle saltation

4.1 Typical saltation dynamic process of a particle

Figure 5 shows the time evolution of a typical continuous saltation of a particle which almost moves through the whole computational domain in the stream-wise direction. About ten obvious hops were observed in $20T_p$, where

Table 4 Comparison of particle saltation statistics between experimental data and numerical results

Variables	Niño & García [6]	Abbott & Francis [4]	Luque & van Beek [33]	Niño et al. [7]	Present results
D	0.5 mm	8.28 mm	0.9 and 3.3 mm	gravel	–
Re_D^+	10.6	523	19.9 and 150	–	100
Θ_c	0.05	0.06	0.05 and 0.06	–	0.06
s_s	2.65	2.57	2.64	–	2.65
τ_w/τ_{wc}	1.03	1.08	1.01 and 1.03	–	1.06
λ_s/D	6.43±3.18	5.93	–	–	6.59±2.71
h_s/D	1.01±0.32	1.03	–	–	0.86±0.24
u_s/u_τ	5.95±1.85	–	3.44 (Regression equation) 3.67 (D = 3.3 mm) 4.26 (D = 0.9 mm)	–	3.61±1.26
θ_r (°)	27.0±14.5	–	–	39.0	40.5±24.1
θ_i (°)	13.8±11.4	–	–	25.1	25.2±9.19
μ_d	0.159±0.281	–	–	–	0.158±0.148

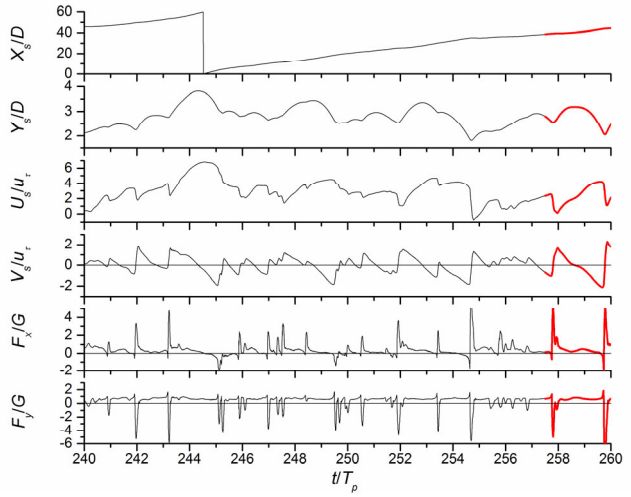

Figure 5 (Color online) Dynamic responses of a particle during typical continuous particle saltations. X_s and Y_s indicate the stream-wise and vertical coordinates of the particle, respectively, U_s and V_s represent the stream-wise and vertical velocities of the particle, respectively, and F_x and F_y are the drag and lift forces, respectively. Coordinates, velocities and forces are non-dimensionalized by particle diatmeter D, bed friction velocity u_τ and submerged gravitational force of the particle G. Time is non-dimensionalized by $T_p = D/u_\tau$. The jump in the stream-wise coordinate curve is due to the periodic boundary conditions in which particles moving out of the right boundary of the computational domain were artificially placed at the left boundary. The last saltation is indicated by thicker solid lines in red.

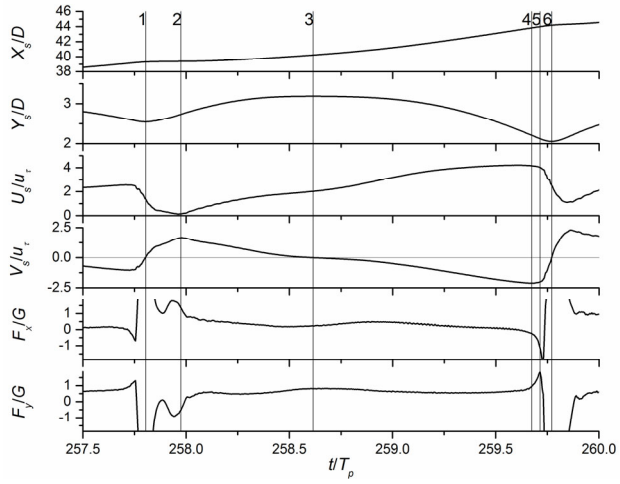

Figure 6 Particle dynamic responses during a typical saltation. The saltation is selected as the last one in Figure 5. The vertical lines indicate six critical instances in time.

$T_p = D/u_\tau$ is a microscopic time scale related to the turbulent flow bed shear stress ($\tau_w = \rho u_\tau^2$) and particle diameter, and is thus suitable for investigation of the details of the interaction between turbulence and particle motion. As shown in Figure 5, each saltation begins at a collision identified by a large negative peak in the vertical hydrodynamic force (lift force) curve and a large positive peak in the stream-wise hydrodynamic force (drag force) curve. Meanwhile, the vertical velocity changes from negative to positive and the vertical coordinate of the particle becomes a local minimum.

The vertical velocity decreased linearly between two successive collisions despite small fluctuations caused by turbulence coherent structures and the interference from other passing-by particles. The effects of turbulence coherent structures are less important for the continuous saltation of large particles than those of smaller ones as in Niño and García [5]. Large particles obtain vertical momentum mainly from their stream-wise momentum at collision, which can be deduced from the strong correlation between the abrupt decrease in the stream-wise velocity and the sudden increase in the vertical velocity. The turbulent structures only cause small fluctuations in the hydrodynamic force and velocity curves.

To clearly demonstrate the saltation process, a typical saltation ($257.5 < t/T_p < 260$) (see Figure 6) has been extracted from Figure 5. Six critical instances in time, indicated by the vertical lines in Figure 6, are selected while corresponding particle positions and pressure distribution on particle surface are presented in Figure 7.

The first instance the authors have chosen is when the vertical velocity of the particle changes from negative to positive and corresponds to the beginning of a saltation. At this time, the particle reaches its lowest position in a saltation and the drag and lift forces reach their positive and negative peaks respectively. Figure 7(a) clearly shows a low pressure region under the bottom of the particle and a high pressure region on the top windward side of the particle.

The second chosen moment in time corresponds to the instant when the vertical velocity reaches its maximum and the stream-wise velocity reaches its minimum. This could be recognized as the end of collision and the beginning of free-flying of the particle. The velocity difference between the fluid and the rebounding particle is so large that a significant flow separation and the resulting low pressure at the top leeside of the particle are observed, as shown in Figure 7(b). The small fluctuations in the drag and lift force curves are caused by vortex shedding in the wake. However, not all the saltations have these kinds of force fluctuations which depend upon the particle's rebounding velocity and the surrounding turbulent flow.

Instance 3 is for the free-flying stage during which only turbulence structures affect the particle's hydrodynamic forces. As shown in Figure 7(c), a low pressure region related with turbulence structures is passing by the moving particle. This causes a larger lift force and a smaller drag force on the particle. Apart from the effect of the turbulence fluctuations, the lift force is almost constant in the whole free-flying stage. The mean non-dimensional lift force is about 0.6 in our case, which means that the lift force is much smaller than the submerged weight.

Instance 4 is characterised with the largest negative vertical velocity and can be considered as the end of free-flying and the beginning of the collision. As regards the decreasing

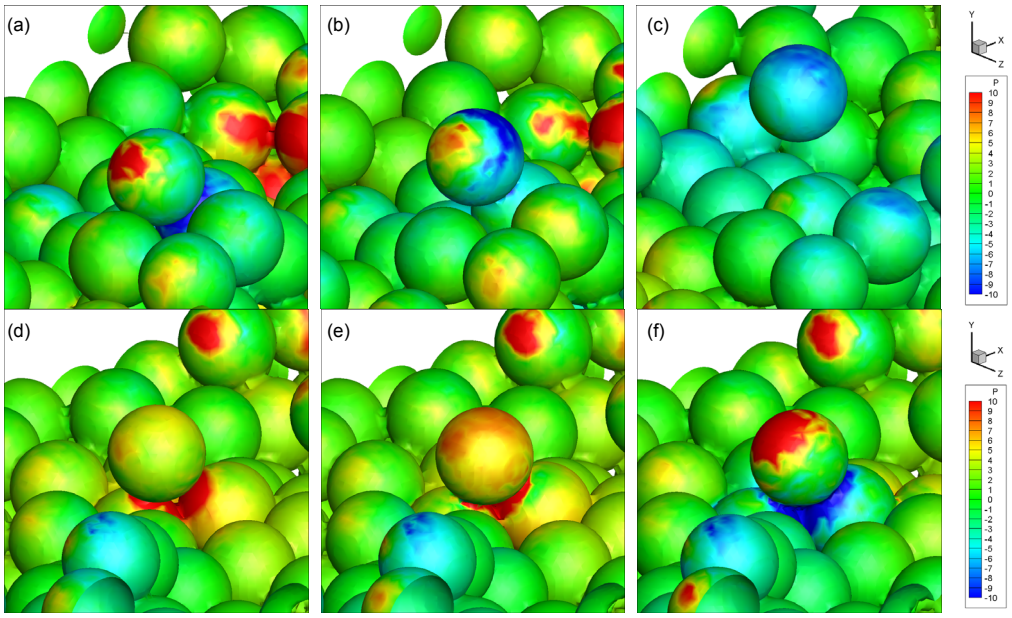

Figure 7 Pressure contours on particle surface during a typical saltation. Time of the sequence corresponds to the six critical instances in Figure 6.

drag force and increasing lift force at this moment, the reason could be that the landing particles are likely to hit the upstream side of the bed particles (as discussed in Section 4.2) and the resulting high pressure in the gaps, as shown in Figure 7(d), generates a negative drag force and a positive lift force.

Instance 5 corresponds to the small negative and positive peaks in the drag and lift force curves, respectively. The pressure distribution at this moment is similar to that of instance 4 except that a slightly high pressure is observed on the top particle surface, as shown in Figure 7(e), due to the deceleration of the particle in the stream-wise direction.

Instance 6 is the beginning of the subsequent saltation and the pressure distribution, as shown in Figure 7(f), is similar to that of instance 1.

The continuous saltation observed in this study supports the conclusions of N&G in that collision-rebounding is possible but disagrees with the statements of Gordon et al. [34] and A&F denying such a possibility. Gordon et al. [34] found in their 'one-dimensional' particle saltation experiments that a moving particle generally did not bounce off a stationary one on the rough bed, but rolled over it for some distance. A&F stated: clear rebounding, without rolling, is rare, and that most take-off velocities at the start of a trajectory are uninfluenced by the previous impact. These are contrary to our findings and the discrepancy could be due to the different particle densities used in these studies. In the experiments of A&F, various particle-fluid density ratios from 1.2 to 2.6 have been tried. Gordon et al. [34] investigated plastic particles with a density ratio of 1.3. However, in our study and the study of N&G, the density ratio is 2.65. Smaller densities lead to smaller particle inertias which causes the particles to be less able to overcome the hydrodynamic resistance (mainly due to the lubrication effects of the thin interstitial fluid film when two particles collide) and thus tend to slide and roll. The side-wall effects of the 'one-dimensional' experiments (Gordon et al. [34]) carried out in a flume with two side walls placed only about one particle diameter from each other for easy observation could be another possible reason for the resulting significant fluid damping.

4.2 Statistical features of particle saltation

As stated in Section 4.1, the beginning and end of a saltation are defined as instances 1 and 6 when the vertical velocity increases from negative to positive. A saltation is further divided into two stages, i.e. the free-flying stage (instance 2 to instance 4) and the collision stage (instance 4 to instance 2 of the subsequent saltation), as shown in Figure 6. In a time period of $60T_p$ after the sediment transport and the turbulent flow are statistically stable, a total of 7312 significant particle hops were observed and various statistical features were calculated based on these samples. However, to discriminate the particle saltation from the particle fluctuation near a balanced position, a criterion was applied that the vertical component of the contact force of the colliding particles at the beginning of a saltation should be larger than 1.5 times of its submerged weight. To verify that our selection of the criteria was not arbitrary, different values of the criteria, from 1.2 to 3.0 times of the submerged weight, were investigated and little difference of the statistical features was observed.

To facilitate the discussions below, an illustration of particle saltation, together with the definitions of characteristic parameters, is shown in Figure 8.

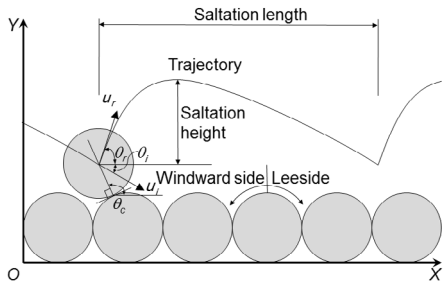

Figure 8 An illustration of particle saltation. u_i and u_r are the incident and rebound velocities, respectively. θ_i, θ_r and θ_c are the incident, rebound and collision angles, respectively.

Figure 9 shows a semi-logarithmic plot of the PDF of the non-dimensional time-span of the free-flying and collision stages. In order to present the probability distribution of the time-span, the non-dimensional time t/T_p (x-axis) is divided into a series of bins, each one with a size of 0.08. The PDF is then calculated as the frequency of the free-flying and collision time-spans that fit into one of the bins - the sum of the probability over all the bins is unity. The mean normalized time-span of the free-flying stage is $t_f/T_p \approx 1.4$ which is larger than the one with the largest probability ($t_f/T_p \approx 1.04$) and the PDF is therefore positively skewed. Similar results can be observed for the collision time-span with the two values of $t_c/T_p \approx 0.4$ and $t_c/T_p \approx 0.3$. The time-span of the whole saltation is calculated as $t_s/T_p = (t_f + t_c)/T_p \approx 1.8$. It should be noted that the time-span for the physical collision of particles is smaller than the collision time-span defined above, because the collision time-span defined in this paper also includes the time for a landing particle approaching the rough bed before physical contact occurs and the time for vortex separation which further increases the vertical velocity (see instance 2 in Figure 6). However, as we are only concerned about the averaged collision features instead of the very short-time physical collision itself, this definition of the collision time-span is reasonable.

Figure 10 shows the PDFs of the non-dimensional saltation velocity u_s/u_τ, incident velocity u_i/u_τ and rebound velocity u_r/u_τ. The incident velocity u_i and the rebound velocity u_r are defined as the particle velocity magnitude at instances 2 and 4 (see Figure 6), respectively, while the saltation velocity u_s is calculated as the particle saltation length λ_s divided by the saltation time-span t_s. Clearly, all the three PDFs are positively skewed which means the particles are more likely to have a larger velocity than having a smaller one, with respect to their mean values of $u_i/u_\tau \approx 4.25$, $u_r/u_\tau \approx 2.92$ and $u_s/u_\tau \approx 3.61$. When $u/u_\tau > 4$ (u can be any of u_i, u_r and u_s), it is observed that $u_i > u_s > u_r$ at any specific probability level, i.e. at any specific velocity, $p(u_i) > p(u_s) > p(u_r)$. The reason can be attributed to the fact that after rebounding from the rough bed, saltating particles are accelerated by the turbulent flow during the free-flying stage, and thus reach a higher velocity when they land again. However, for a saltation with a low velocity of $u/u_\tau < 2$, the saltation velocity u_s is consistently smaller than the other two counterparts. To explain this result, it is worth mentioning again that u_i and u_r are the magnitudes of the landing and rebounding velocity vectors while u_s is the mean value of the stream-wise velocity component during a saltation. A fast-moving particle predominantly moves in the stream-wise direction and the resultant particle velocity is approximately equal to the saltation velocity. While, for a slow-moving particle, the vertical component of the resultant velocity is comparable to the stream-wise one and thus cannot be neglected. However, in the definition of the saltation velocity, the vertical component is not considered which leads to a smaller u_s when $u/u_\tau < 2$.

Figure 11 shows the PDFs of the incident angle θ_i, rebound angle θ_r and collision angle θ_c. The PDFs of θ_i

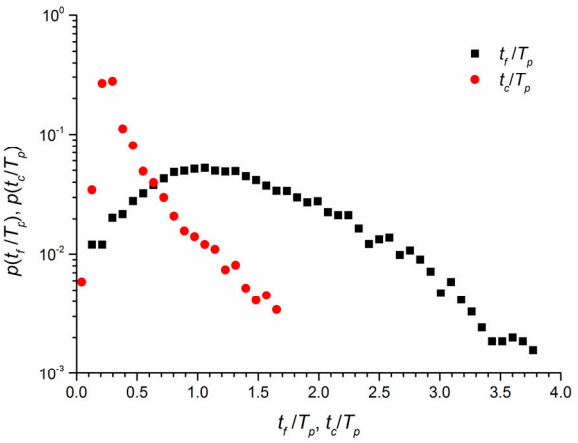

Figure 9 (Color online) The probability density function (PDF) of the time-span of the free-flying and collision stages. The bin size is 0.08.

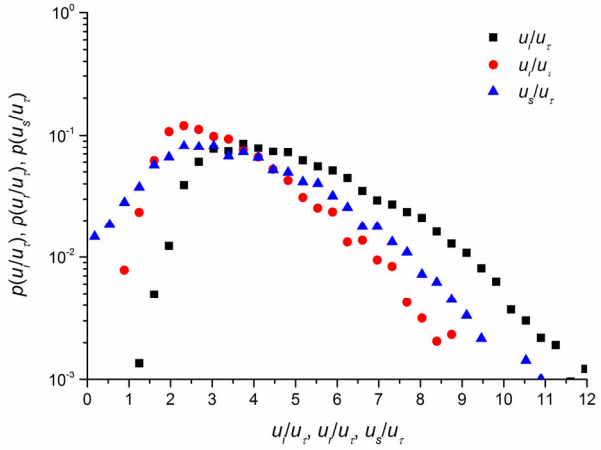

Figure 10 (Color online) The probability density function (PDF) of the incident, rebound and saltation velocities. The bin size is 0.3.

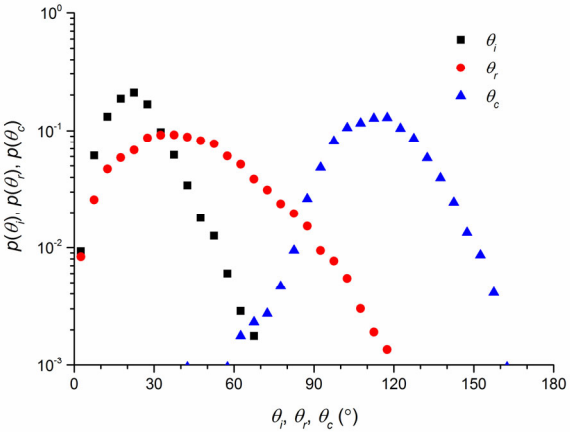

Figure 11 (Color online) The probability density function (PDF) of the incident, rebound and collision angles. The bin size is 5°.

and θ_r are positively skewed while the PDF of θ_c is approximately symmetric. The mean values and standard deviations of the incident and rebound angles are listed in Table 4. A larger value of the standard deviation of the rebound angle means that it is more scattered than the incident angle. This can be attributed to the fact that the rebound angle is closely related to the collision angle between the saltating particles and the randomly packed bed particles, while the incident angle is mainly influenced by the turbulent flow and thus more concentrated. The collision angle shows a Gaussian distribution despite small fluctuations near the lower end due to insufficient sampling there. It is also found that the cumulative probability for $\theta_c < 90°$ is much smaller than that for $\theta_c > 90°$ which means the landing particles are more likely to hit the upstream side of the bed particles.

To investigate the influence of incident angle, the relationships between θ_r (θ_c and u_{rv}/u_τ) and θ_i are presented in Figure 12, where u_{rv}/u_τ is the vertical component of the non-dimensional rebound velocity. Mean values of θ_r, θ_c and u_{rv}/u_τ are plotted with their corresponding θ_i falling into a series of bins. It can be observed that θ_r increases linearly with increasing θ_i, while θ_c shows a rather insignificant dependency on θ_i. The normalized vertical rebound velocity peaks at $\theta_i = 22.5°$ which coincides with the incident angle of the largest probability. The fluctuations at $\theta_i > 50°$ are obviously caused by insufficient sampling as shown in Figure 11.

To further investigate the effects of local rough-bed packing on particle saltation, we calculated and plotted the mean value of u_{rv}/u_τ for each collision angle (see Figure 13). Clearly, the vertical velocity of rebounding particles hitting the windward side of bed particles is larger than the one of rebounding particles hitting the leeside. Furthermore, we averaged the vertical velocities for all windward-side and leeside bins respectively and found that the normalized mean vertical velocity of the rebounding particles hitting the windward side is 1.29 and the normalized mean vertical velocity of the rebounding particles hitting the leeside is 0.77. This result shows that the saltating particles hitting the windward side of bed particles are more likely to rebound from the rough bed than those hitting the leeside.

4.3 Mechanisms of particle saltation

The mechanisms for the entrainment from rest and the subsequent continuous saltation of large grain-size particles are different. As shown in Ji et al. [32] and Dwivedi et al. [35], turbulence coherent structures, especially sweep structures, play a significant role in the incipience of sediment entrainment. Large particles are expelled off the rough bed by the pressure gradient generated by turbulence structures. However, for the subsequent continuous saltation in this study, the collision parameters, such as incident angle, local rough bed packing arrangement and particle density, etc., are crucial. The generated contact force can be one order of

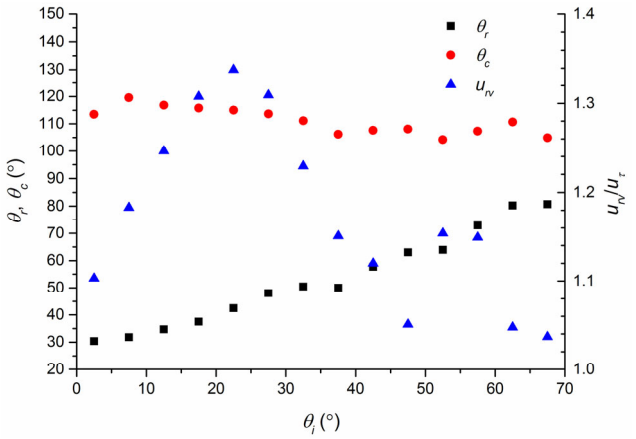

Figure 12 The dependency of the rebound angle θ_r, the collision angle θ_c and the normalized vertical rebound velocity u_{rv}/u_τ on the incident angle θ_i. Plotted values represent the means of θ_r, θ_c and u_{rv}/u_τ in a series of θ_i-bins with a size of 5°.

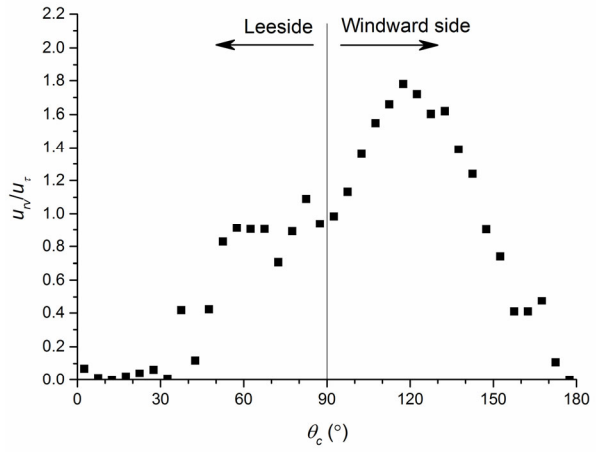

Figure 13 The relationships between the collision angle θ_c and the normalized vertical rebound velocity u_{rv}/u_τ. Plotted values represent the means of u_{rv}/u_τ in a series of θ_c-bins with a size of 5°. The vertical solid line divides the plane into leeside and windward side.

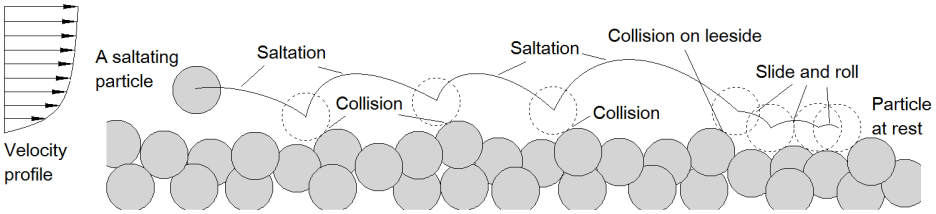

Figure 14 Schematic diagram of the saltation mechanisms of large grain-size particles.

magnitude larger than the hydrodynamic force caused by the turbulence structures as shown in Figures 5 and 6. However, this does not mean that the influence of turbulence structures is negligible. Turbulence structures modify the hydrodynamic forces on particles during the free-flying stage and thus affect saltation height and length.

As stated above, the gain in the upward momentum of a saltating particle is obtained from the loss of its stream-wise momentum at collision. So if there is not a significant collision between the particle and the rough bed, i.e., for example, if the particle hits the top leeside of a rough bed particle, the particle cannot obtain enough upward momentum to rebound from the rough bed (as shown in Figure 12) and tends to slide on or roll over the bed particles. Because the particle cannot obtain enough stream-wise momentum due to the lower flow velocity in the vicinity of the bed and the sheltering effects of the upstream bed particles, it will finally settle down. This dynamic process is shown in Figure 14. This particle will keep stationary until it is entrained by a strong passing-by turbulence structure.

5 Conclusions

In this study, the particle saltation in turbulent channel flow has been numerically investigated. The methodology adopted is a combination of the direct numerical simulation (DNS) of the turbulent flow, the combined finite-discrete element method (FDEM) for the particle dynamics, and the immersed boundary method (IBM) for the fluid-solid interactions. The statistical features of turbulent flow over a fixed rough bed show good agreement with published experimental data and numerical results. Various particle saltation statistics were investigated and excellent agreement with experimental data has been achieved. Following statistical validation of the turbulent flow and particle transport, a complete dynamical process of continuous particle saltation, together with surrounding turbulent flow, has been presented for the first time. The strong correlation between the abrupt changes in particle stream-wise and vertical velocity indicates that the particle's upward momentum is transferred from the stream-wise momentum by particle-bed collisions. This clearly shows a different physical process compared with that of particle entrainment from rest in which a particle's upward momentum is obtained from turbulent coherent structures. The probability distribution function of several important particle saltation parameters and the relationships between them have been investigated. The vertical rebound (lift-off) velocity was evaluated as a function of the collision angle and the results show that saltating particles hitting the windward side of the bed particles are more likely to bounce off the rough bed than those hitting the leeside. Finally, the saltation mechanisms of large grain-size particles in turbulent channel flow have been presented.

With the use of state-of-the-art techniques of computational fluid dynamics and computational mechanics of discontinua, this numerical study has shed new light on the complicated saltation motion near the rough-bed surface in turbulent channel flow, and will be helpful to enhancing the formulation of theoretical models.

This work was supported by a Marie Curie International Incoming Fellowship within the seventh European Community Framework Programme (Grant No. PIIF-GA-2009-236457). The first author acknowledges the financial support of the Science Fund for Creative Research Groups of the National Natural Science Foundation of China (Grant No. 51321065), Programme of Introducing Talents of Discipline to Universities (Grant No. B14012), National Natural Science Foundation of China (Grant Nos. 50809047 and 51009105) and Natural Science Foundation of Tianjin (Grant No. 12JCQNJC02600). We thank UKTC for HECToR computer time and facilities.

1 Niño Y, García M. Gravel saltation: 2. Modeling. Water Resour Res, 1994, 30: 1915–1924
2 Bialik R J, Nikora V I, Rowinski P M, et al. A numerical study of turbulence influence on saltating grains. In: Dittrich A, Koll K, Aberle J Geisenhainer P, eds. Proceedings of International Conference on Fluvial Hydraulics (River Flow 2010), Braunschweig, Germany, 2010. 105–112
3 van Rijn L C. Sediment transport, part I: bed load transport. J Hydraul Eng-ASCE, 1984, 110: 1431–1456
4 Abbott J E, Francis J R D. Saltation and suspension trajectories of solid grains in a water stream. Phil Trans R Soc Lond A, 1977, 284: 225–254
5 Niño Y, García M H. Experiments on particle–turbulence interactions in the near–wall region of an open channel flow: implications for sediment transport. J Fluid Mech, 1996, 326: 285–319
6 Niño Y, García M H. Experiments on saltation of sand in water. J Hydraul Eng - ASCE, 1998, 124: 1014–1025
7 Niño Y, García M, Ayala L. Gravel saltation: 1. Experiments. Water Resour Res, 1994, 30: 1907–1914
8 Lee H Y, Hsu I S. Investigation of saltating particle motions. J Hydraul Eng - ASCE, 1994, 120: 831–845
9 Lee H Y, Chen Y H, You J Y, et al. Investigations of continuous bed load saltating process. J Hydraul Eng-ASCE, 2000, 126: 691–700

10 Lee H Y, You J Y, Lin Y T. Continuous saltating process of multiple sediment particles. J Hydraul Eng - ASCE, 2002, 128: 443–450
11 Ancey C, Bigillon F, Frey P, et al. Saltating motion of a bead in a rapid water stream. Physical review E, 2002, 66: 036306
12 Ancey C, Böhm T, Jodeau M, et al. Statistical description of sediment transport experiments. Physical Review E, 2006, 74: 011302
13 Osanloo F, Kolahchi M R, McNamara S, et al. Sediment transport in the saltation regime. Physical Review E, 2008, 78: 011301
14 Niño Y, García M. Using Lagrangian particle saltation observations for bedload sediment transport modeling. Hydrological Processes, 1998, 12: 1197–1218
15 Chan-Braun C, Garcia-Villalba M, Uhlmann M. Force and torque acting on particles in a transitionally rough open channel flow. J Fluid Mech, 2011, 684: 441–474
16 Chan-Braun C, Garcia-Villalba M, Uhlmann M. Direct numerical simulation of sediment transport in turbulent open channel flow. In: Nagel W E, Kröner D B, Resch M M, eds. High Performance Computing in Science and Engineering'10. Heidelberg: Springer, 2011. 295–306
17 Thomas T G, Williams J J R. The development of a parallel code to simulate skewed flow over a bluff body. J Wind Eng Ind Aero, 1997, 67-68: 155–167
18 Singh K M, Sandham N D, Williams J J R. Numerical simulation of flow over a rough bed. J Hydraul Eng - ASCE, 2007, 133: 386–398
19 Ma J, Williams J J R. Implication of horizontal force moments for the threshold of bed entrainment in an open-channel flow. J Hydro-environ Res, 2009, 3: 2–8
20 Peskin C S. Flow patterns around heart valves: a numerical method. J Comp Phys, 1972, 10: 252–271
21 Ji C, Munjiza A, Williams J J R. A novel iterative direct-forcing immersed boundary method and its finite volume applications. J Comp Phys, 2012, 231: 1797–1821
22 Munjiza A, Owen D R J, Bicanic N. A combined finite-discrete element method in transient dynamics of fracturing solids. Eng Comp, 1995, 12: 145–174
23 Munjiza A, Andrews K R F. Penalty function method for combined finite-discrete element systems comprising large number of separate bodies. Int J Numer Meth Eng, 2000, 49: 1377–1396
24 Xiang J, Munjiza A, Latham J P, et al. On the validation of DEM and FEM/DEM models in 2D and 3D. Eng Comp: Int J Comp-Aided Eng, 2009, 26: 673–687
25 Hofland B. Rock and roll, turbulence-induced damage to granular bed protections. Dissertation of the Doctoral Degree. Delft: Delft University of Technology, 2005
26 Defina A. Transverse spacing of low-speed streaks in a channel flow over a rough bed. In: Ashworth P J, Bennett S J, Best J L, et al., eds. Coherent Flow Structures in Open Channels. New York: Wiley, 1996. 87–99
27 Grass A J, Stuart R J, Mansour-Tehrani M. Vortical structures and coherent motion in turbulent flow over smooth and rough boundaries. Philos Trans R Soc London, Ser. A, 1991, 336: 33–65
28 Grass A J. Structural features of turbulent flow over smooth and rough boundaries. J Fluid Mech, 1971, 50: 233–255
29 Nezu I. Turbulence structure in an open channel flow. Dissertation of the Doctoral Degree. Kyoto: Kyoto University, 1977
30 Nezu I, Nakagawa H. Turbulence in Open-channel Flows. Rotterdam: Balkema, 1993
31 Jiménez J. Turbulent flows over rough walls. Annu Rev Fluid Mech, 2004, 36: 173–196
32 Ji C, Munjiza A, Avital E, et al. Direct numerical simulation of sediment entrainment in turbulent channel flow. Phys Fluids, 2013, 25: 056601
33 Luque R F, van Beek R. Erosion and transport of bed-load sediment. J Hydrol Res, 1976, 14: 127–144
34 Gordon R, Carmichael J B, Isackson F J. Saltation of plastic balls in a 'one-dimensional' flume. Water Resour Res, 1972, 8: 444–459
35 Dwivedi A, Melville B W, Shamseldin A Y, et al. Flow structures and hydrodynamic force during sediment entrainment. Water Resour Res, 2011, 47: W01509